

RESEARCH ARTICLE

Full-waveform inversion of the Japanese Islands region

10.1002/2016JB012802

Key Points:

- Three-dimensional full seismic waveform model of the Japanese Islands region for 20–80 s period constructed via spectral-element and adjoint methods
- The model shows low v_s anomaly reaching –19% at 100 km depth beneath the Ulleung volcanic island (Sea of Japan)
- This anomaly is interpreted as upwelling from the Pacific slab at 400 km depth, possibly related to fluids

Correspondence to:

S. Simutè,
saule.simute@erdw.ethz.ch

Citation:

Simutè, S., H. Steptoe, L. Cobden, A. Gokhberg, and A. Fichtner (2016), Full-waveform inversion of the Japanese Islands region, *J. Geophys. Res. Solid Earth*, 121, 3722–3741, doi:10.1002/2016JB012802.

Received 9 JAN 2016

Accepted 5 MAY 2016

Accepted article online 10 MAY 2016

Published online 31 MAY 2016

Saulè Simutè¹, Hamish Steptoe², Laura Cobden², Alexey Gokhberg¹, and Andreas Fichtner¹

¹Department of Earth Sciences, ETH Zurich, Zurich, Switzerland, ²Department of Earth Sciences, Utrecht University, Utrecht, Netherlands

Abstract We present a full-waveform tomographic model of the crust and upper mantle beneath the Japanese Islands region. This is based on the combination of GPU-accelerated spectral-element wavefield simulations, adjoint techniques, and nonlinear optimization. Our model explains complete seismic waveforms of events not used in the inversion in the period range from 20 to 80 s. Quantitative resolution analysis indicates that resolution lengths within the well-covered areas are around 150 km in the horizontal and around 30 km in the vertical directions. In addition to the high-velocity signatures of known lithospheric slabs in the region, our model reveals a pronounced low-velocity anomaly beneath the volcanic island of Ulleung in the Sea of Japan, reaching –19% around 100 km depth. The Ulleung anomaly originates at or above the Pacific slab, rises vertically upward to the base of the Philippine Sea slab at ~200 km depth, circumvents it in NW direction, and then significantly strengthens in the uppermost mantle above the Philippine Sea slab. Among the numerous hypotheses for the generation of low-velocity anomalies in subduction systems, those invoking instabilities before or when a slab enters the transition zone seem most likely. The age and fast subduction of the Pacific slab may facilitate the transport of fluids into the transition zone. This may promote the reduction in viscosity and the onset of convective upwelling, aided by ambient mantle flow, such as return flow within the mantle wedge.

1. Introduction

1.1. The Japanese Islands Region

The Japanese Islands are a volcanic arc system consisting of several thousand islands, with Hokkaido, Honshu, Shikoku, and Kyushu being the largest (Figure 1). Complex tectonic processes, such as subduction, back-arc spreading, and arc-arc collision led to the formation and current position of the islands. Before ~30 Ma, the Japanese Islands were situated at the eastern margin of continental Asia, with the active plate boundary in the east due to the subduction of the Pacific plate [Jolivet *et al.*, 1994; Wakita, 2013]. The opening of the Sea of Japan (also known as the East Sea) initiated around 30 Ma and lasted until the mid-Miocene (~15 Ma), when the extension changed to compression in response to the arc-arc collision of the Izu-Bonin arc against southwestern Japan [Hall, 2002; Ingle, 1992; Jolivet *et al.*, 1994; Itoh, 1988]. The arc-arc collision led to a complex triple junction currently situated off the east coast of central Japan [Taira, 2001]. The opening of the Sea of Japan allowed for the formation of three deep basins—the Japan, Yamato, and Ulleung—separated by topographic highs and reaching 2–3 km depth [Ingle, 1992]. A number of seamounts are situated on the sea floor of the Sea of Japan, but only a few volcanic islands rise above the water surface [Kim *et al.*, 1999]. These are Ulleung (Korean 울릉도, also known as Ulleung-do or Ulleungdo), Dokdo, and Oki Islands in the southwestern Sea of Japan. There are no dated eruptions for the Dokdo or Oki Islands [Siebert *et al.*, 2010], while volcanism at Ulleung lasted intermittently since the Pleistocene (~1.4 Ma) until the mid-Holocene (~5 ka B.P.) [Kim *et al.*, 1999]. The origin of Ulleung volcano, however, remains elusive, and several models have been proposed to explain magmatic activity in the back-arc region.

Currently, interactions between the Eurasian, North American, Pacific, and Philippine Sea plates shape the tectonics of the Japanese Islands region. Further complications are added by the presence of various microplates, including the Amur, Yangtze, and Okhotsk plates [Bird, 2003]. Subduction of the Pacific plate beneath the North American plate takes place along the Kuril and Japan trenches, while its subduction beneath the Philippine Sea plate occurs at the Izu-Bonin trench. The Pacific slab reaches the mantle transition zone beneath the Sea of Japan and becomes stagnant there [Lei and Zhao, 2005; Huang and Zhao, 2006; Li and van der Hilst, 2010; Wei *et al.*, 2015]. Besides, the northwestern margin of the Philippine Sea plate is subducting beneath

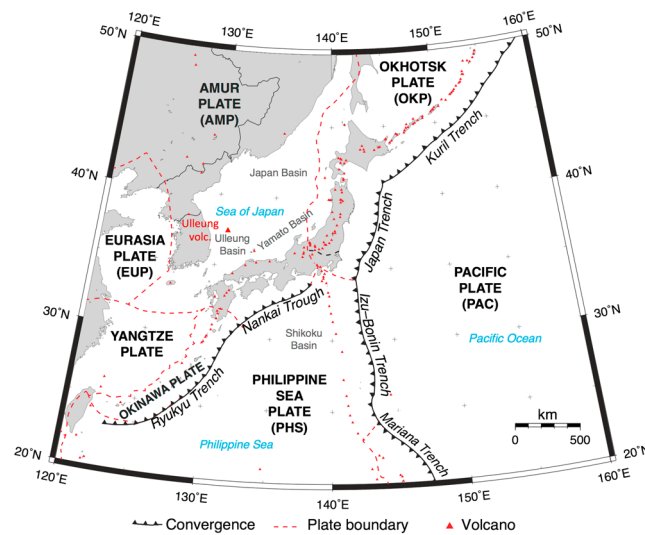


Figure 1. Tectonic setting of the Japanese Island arc system. Locations of plate boundaries are taken from *Bird* [2003], and locations of Holocene volcanoes from *Siebert et al.* [2010].

the Eurasian plate. The presence of the Pacific and Philippine Sea slabs in the southwestern part of the Sea of Japan is likely to have an effect on the upper mantle processes in the area.

1.2. Motivation

As a result of the tectonic activity outlined in the previous paragraph, the crust and mantle beneath the Japanese Islands are highly heterogeneous. Ocean-continent transitions cause strong lateral contrasts, and additional variations in elastic properties are expected from the presence of subducting slabs, volcanic arcs, and intraplate volcanoes. The complexity of the region complicates the discovery of 3-D Earth structure and the accurate characterization of large earthquake rupture processes.

Elastic property contrasts over distances of a few wavelengths or less decrease the accuracy of the ray approximation [*Cerveny*, 2001], frequently used in tomographic studies. Crustal corrections for surface waves lose their accuracy at periods below ~ 60 s, needed to constrain regional-scale Earth structure [*Bozdağ and Trampert*, 2008]. Tomography in strongly heterogeneous regions is further complicated by strong nonlinearity that must be taken into account through iterative improvements of the Earth model.

Inferences of earthquake rupture processes can be severely polluted by neglecting 3-D Earth structure in finite-source inversions [e.g., *Graves and Wald*, 2001; *Razafindrakoto and Mai*, 2014; *Gallovic et al.*, 2015]. Simplified layered Earth models—most often used in finite-source studies [e.g., *Archuleta*, 1984; *Cotton and Campillo*, 1995]—may not reproduce the seismic waveform complexities induced by structural heterogeneity, especially at higher frequencies. To avoid artifacts, the exploitable frequency band must often be limited to lower frequencies, thereby contributing to the notorious nonuniqueness of finite earthquake source inversions [*Mai and Thingbaijam*, 2014].

To address these challenges, we perform a full seismic waveform inversion of the crust and upper mantle beneath the Japanese Islands region. This is intended to produce a 3-D Earth model that does not suffer from approximations in the seismic forward problem solution and may be used in future earthquake source inversions.

1.3. Outline

This paper is organized as follows: We begin in section 2 with the description of seismic data used in this study. Section 3 is dedicated to the methodology applied in our full-waveform inversion. We briefly describe the initial model and the forward modeling, followed by the quantification of waveform differences and the details of the iterative optimization. Results are presented in section 4, where we assess our model in terms of its ability to explain waveforms not used in the inversion, and in terms of quantitative resolution estimates obtained by random probing techniques. The tomographic results in terms of lateral averages, isotropic S velocity structure and radial anisotropy are presented in section 4.3. In section 5 we discuss physical implications of a pronounced low-velocity anomaly beneath the Ulleung basin and evaluate the main hypothesis regarding its origin. We further discuss advantages and shortfalls of our approach in section 5 and summarize the main conclusions in section 6.

2. Data

Within the model domain, we selected 58 earthquakes, distributed spatially as uniformly as possible, and with magnitudes ranging between M_w 5.0 and 6.9 (Figure 2). We obtained waveform data from all freely available seismic networks in the area, namely, the Full Range Seismograph Network of Japan

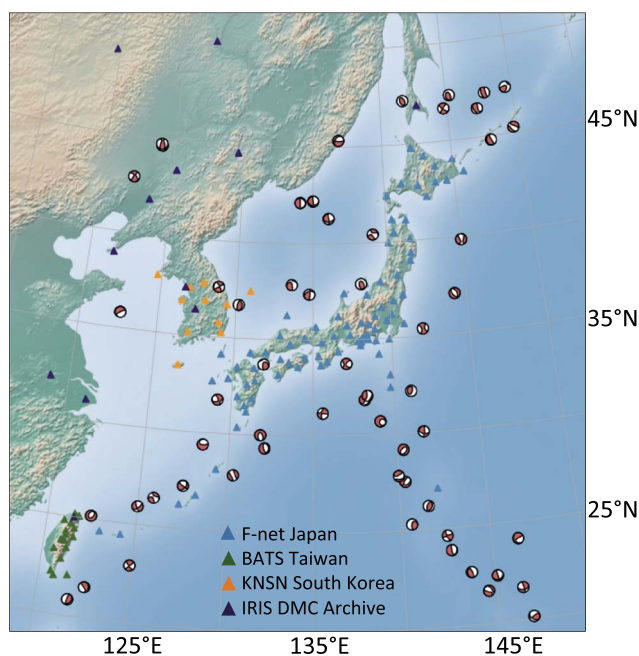


Figure 2. Distribution of stations (triangles) and earthquake epicenters, plotted as beachballs that indicate the source mechanism.

(F-Net, <http://www.fnet.bosai.go.jp>), the Broadband Array in Taiwan for Seismology (BATS, <http://bats.earth.sinica.edu.tw>), the Korea National Seismograph Network (KNSN, <http://www.kma.go.kr/weather/earthquake/internationalist.jsp>), and several stations from the China National Seismic Network, the New China Digital Seismograph Network, the Global Seismograph Network, and the Korean Seismic Network, made available by the Incorporated Research Institutions for Seismology (IRIS) Data Management Center (<http://ds.iris.edu/ds/nodes/dmc/>).

To enhance the efficiency of the adjoint method-based inversion, explained in section 3.3, we preferred events with a large number of useful recordings. With a total of 165 available seismic stations and 58 events, our final data set contains more than 5500 three-component waveforms. We retrieved earthquake information, including locations and moment tensors, from the National Research Institute for Earth Science and Disaster Prevention Seismic Moment Tensor Catalog, and from the Global Centroid Moment Tensor Catalog, in cases where it was not available in the former [Fukuyama *et al.*, 1998; Ekström *et al.*, 2012].

3. Forward and Inverse Modeling Methods

To derive a 3-D model of the Japanese Islands region from the seismic recordings, we applied full-waveform inversion [e.g., Bamberger *et al.*, 1982; Igel *et al.*, 1996; Pratt, 1999; Chen *et al.*, 2007; Fichtner *et al.*, 2009a; Tape *et al.*, 2010; Colli *et al.*, 2013], described schematically in the workflow shown in Figure 3. Further details concerning the initial model, the forward modeling, the quantification of waveform differences, and the iterative optimization are provided below.

3.1. Initial Model and Forward Modeling

To reduce the risk of converging toward a local minimum, we started the inversion with a 3-D initial model derived from a previous full-waveform inversion at long periods from 50 to 100 s [Diaz-Steptoe, 2013]. The initial model, displayed in Figure 4, describes the long-wavelength structure of SH velocity v_{sh} , SV velocity v_{sv} , isotropic P velocity v_p , and density ρ . Lateral variations in crustal structure are included in the initial model as well. To account for viscoelastic attenuation, we use the Q model QL6 by Durek and Ekström [1996].

For the simulation of seismic wave propagation through 3-D heterogeneous Earth models, we employed a GPU-enabled spectral-element solver of the seismic wave equation [Fichtner *et al.*, 2009b; Gokhberg and Fichtner, 2016]. Widely used in seismological research, the spectral-element method combines the accuracy of pseudo-spectral methods with the geometric flexibility and ease of parallelization of finite-elements

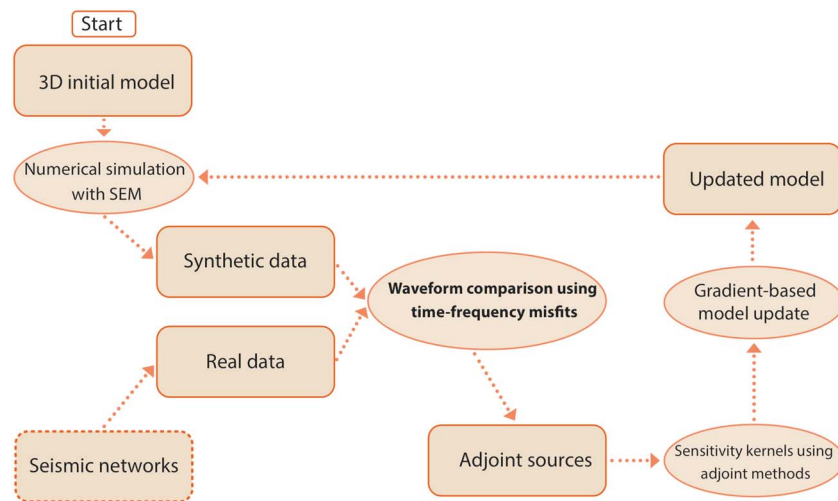


Figure 3. Schematic workflow describing one iteration of a full-waveform inversion. Starting from a suitable initial model, we compare numerically computed and observed waveforms using time-frequency phase misfits [Fichtner et al., 2008]. With the help of adjoint techniques [e.g., Tarantola, 1988; Tromp et al., 2005; Fichtner et al., 2006], we then compute sensitivity kernels that allow us to compute an updated version of the model, with improved fit between observations and synthetics. This procedure is iterated until a satisfactory fit is achieved.

[e.g., Seriani and Priolo, 1994; Priolo et al., 1994; Faccioli et al., 1996; Komatitsch and Vilotte, 1998; Komatitsch and Tromp, 2002]. The solver provides in-built meshing which subdivides the numerical domain into a prescribed number of uniformly sized elements in the spherical coordinate system. In this study, the Earth model and the wavefield are represented by Lagrange polynomials of degree 4, which constitutes a good compromise between accuracy and efficiency [Fichtner, 2010]. To ensure that numerical errors are negligible compared to the observed differences between observed and synthetic seismograms, we used nine grid points per minimum wavelength. Thus, for the 20–80 s period range wavefield simulation, the average grid spacing was 7.5 km in horizontal and 2 km in vertical direction.

3.2. Quantification of Waveform Differences

The quantification of waveform differences is a two-step procedure, consisting of (i) the selection of suitable measurement windows and (ii) the computation of a waveform misfit.

We select measurement windows in a semiautomatic fashion using the *LARge-scale Seismic Inversion Framework* (LASIF) developed by Krischer et al. [2015]. Initially, windows are preselected automatically based on a series of similarity measures, including time-dependent correlation coefficients and amplitude differences. Subsequently, the windows are manually checked and adjusted when needed. In addition to data selection, LASIF is designed to handle large amounts of data and different components of the inversion in a

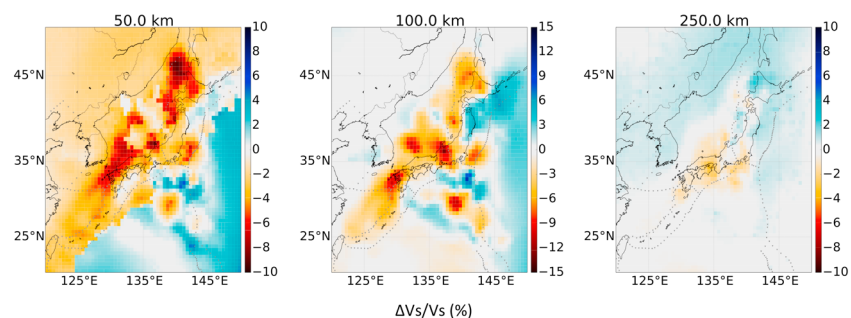


Figure 4. Depth slices of the isotropic *S* velocity perturbation in the initial model taken from the long-period full-waveform inversion of Diaz-Stepto et al. [2013]. For easy comparison with the final results in Figures 10 and 11, the perturbation is also calculated with respect to the 1-D lateral average isotropic *S* velocity of the final model, shown in Figure 9.

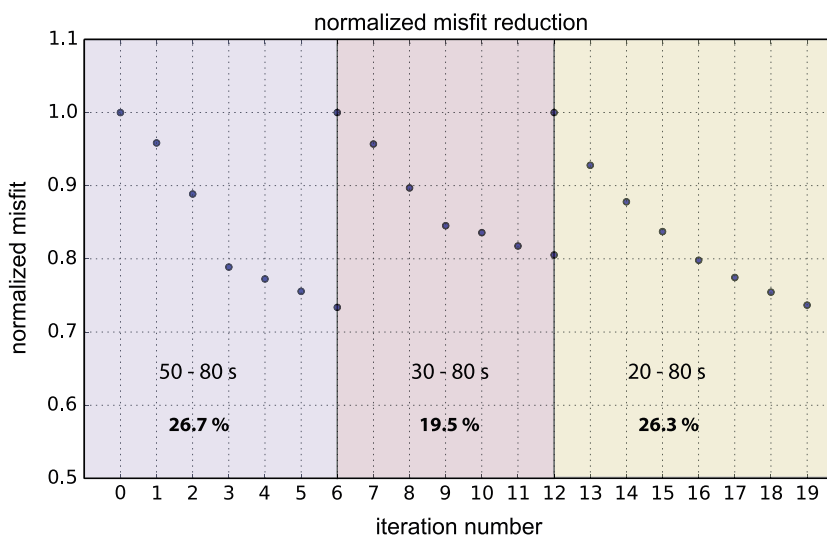


Figure 5. Per-iteration misfit reductions for the three successively broadened period bands of 50–80 s, 30–80 s, and 20–80 s. The decreasing misfit corresponds to the improving fit within the selected time-frequency measurement windows. The misfits are normalized to a maximum of 1 for each period band.

structured fashion. It provides tools to process data, perform measurements, and compute adjoint sources. LASIF links the aforementioned components to the forward and adjoint solvers by reading and writing solver-specific input and output.

To extract information of waveform differences within the windows, we measure time-frequency phase misfits [Fichtner and Igel, 2008]. Being independent of a whole-seismogram amplitude scaling, the phase misfits avoid trade-offs with imperfectly known earthquake magnitudes, while still capturing amplitude differences between neighboring oscillations. Furthermore, the phase misfits do not rely on the identification of specific phases, which are often not well separated at shorter epicentral distances, typical of our study region. The time-frequency misfits allow us to perform measurements on all types of waves recorded on the seismogram. Our measurements include body waves and fundamental- and higher-mode surface waves. Surface waves dominate the recordings at the period range of this study (20–80 s) and, thus, represent the largest part of the measurements.

3.3. Iterative Optimization

Following forward simulations and misfit quantification, we compute sensitivity kernels using adjoint techniques [e.g., Tarantola, 1988; Fichtner et al., 2006; Liu and Tromp, 2008]. The sensitivity kernels drive an iterative conjugate-gradient optimization, where optimal step lengths are computed via a line search. To avoid cycle skipping and convergence toward a local minimum, we adopt a multiscale approach [e.g., Bunks et al., 1995; Fichtner, 2010] that consists of a successive broadening of the period band. We start with long periods from 50 to 80 s. After a satisfactory fit between observations and synthetics is reached, we broaden the period band toward shorter periods, first from 30 to 80 s, and finally from 20 to 80 s. Each broadening of the period band is accompanied by a reselection of the measurement windows.

4. Results

After a total of 19 iterations, we obtained an updated model of the Japanese Islands region, henceforth referred to as \mathbf{m}_{19} . For the three successively broadened period bands of 50–80 s, 30–80 s, and 20–80 s, the misfit decreased in total by 26.7%, 19.5%, and 26.3%, respectively. The per-iteration misfit reductions are shown in Figure 5. A representative example of the waveform fit for individual stations, relative to the one obtained for the initial model, is provided in Figure 6. In the following paragraphs, we present our inversion results, including the fit to data that were not used in the inversion, a quantitative resolution analysis, and a display of isotropic shear velocity structures and radial anisotropy.

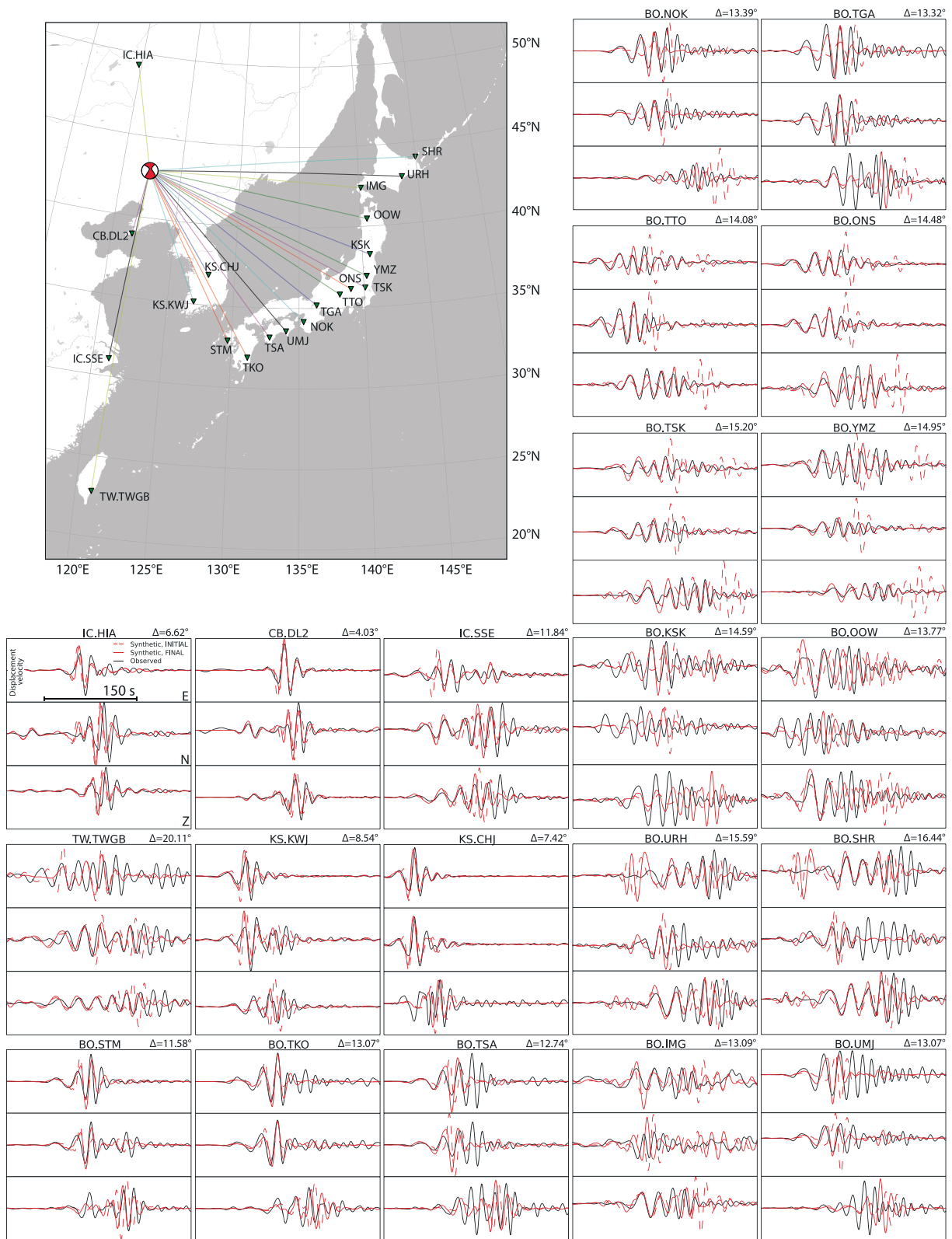


Figure 6. Comparison of the overall fit between the synthetics from the initial model (red dashed), the synthetics from the final model m_{19} (red continuous), and the observed waveforms (black) for an M_w 5.0 event in northeastern China that occurred on 22 April 2013.

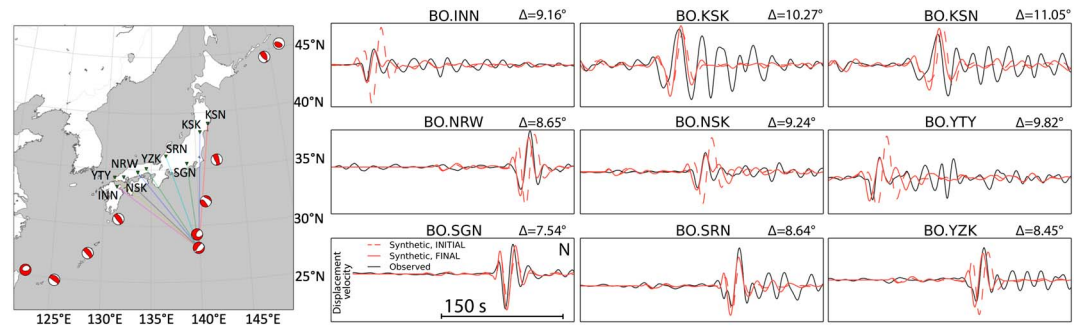


Figure 7. (left) Map showing the distribution of 10 recent events used to assess the ability of the model to explain data not used in the inversion. To be conservative, we did not bias the selection toward high-quality data, in contrast to the events used in the actual inversion. (right) Comparison of the overall waveform fit between synthetics from the initial model (red dashed), synthetics from the final model \mathbf{m}_{19} (red continuous), and the observed waveforms (black) for the event for which raypaths are shown in the map. The M_w 5.4 event occurred near the Bonin Islands on 21 September 2014.

4.1. Waveform Fit for Newly Added Data

The ability of the new model to explain waveform data that were not used in the inversion is critical for applications related to earthquake source inversion and early warning. It furthermore serves as an important tool to identify potential overfitting.

For this analysis of seismogram fit, time-frequency phase misfits [Fichtner *et al.*, 2008] cannot be used, as they produce meaningless results in the presence of cycle skips that may occur in the newly added data that were not specifically preselected for waveform inversion. We therefore adopt the whole-seismogram misfit measure

$$\chi_{\text{all}}(\mathbf{m}) = \frac{\int_0^T [u_i^0(t) - u_i(t, \mathbf{m})]^2 dt}{\sqrt{\int_0^T [u_i^0(t)]^2 dt \int_0^T [u_i(t, \mathbf{m})]^2 dt}} \quad (1)$$

proposed earlier, for instance, by Tape *et al.* [2010]. In equation (1), $u_i^0(t)$ denotes the i component of the observations, $u_i(t, \mathbf{m})$ the i component of the synthetics, and T the duration of the time series. The mean is taken over all stations and components. While the numerical value of an individual χ_{all} depends also on T and on the noise level, the average over data used and not used in the inversion still provides a useful means of objective comparison.

In the period band from 20 to 80 s, the average per-trace misfit $\bar{\chi}_{\text{all}}$ for the data used in the inversion is 1.85. For the 10 newly added events displayed in Figure 7 (left), the average per-trace misfit reaches a value of 1.95. Rather than being an indicator of overfitting, this slightly higher value is most likely the result of not biasing our selection of new events toward events with large numbers of useful recordings, as we did in the selection process for the inverted data. Figure 7 (right) provides a visual impression of the newly added data in relation to the synthetics computed from our initial and final models. From the combination of quantitative and visual analyses, we conclude that the iterative optimization was stopped sufficiently early, that is, before overfitting could occur.

4.2. Quantitative Resolution Analysis

Using resolution analysis by random probing [Fichtner and van Leeuwen, 2015], we computed direction- and position-dependent resolution lengths. These are displayed in Figure 8 for the E-W, N-S, and vertical directions. Resolution analysis by random probing operates by sampling the Hessian of the misfit functional using a small number of (typically five) random test models. This is achieved with the help of second-order adjoints [Santosa and Symes, 1988; Fichtner and Trampert, 2011]. The Hessian-model applications are autocorrelated in different directions, yielding the corresponding direction-dependent resolution lengths. The computational cost of resolution analysis by random probing is equivalent to only ~ 5 conjugate-gradient iterations in the optimization stage of the inversion (section 3.3), i.e., slightly less than 25% of the complete optimization in our case (19 iterations). Resolution lengths are obtained throughout the domain, omitting, however, some boundary regions required by the random probing technique.

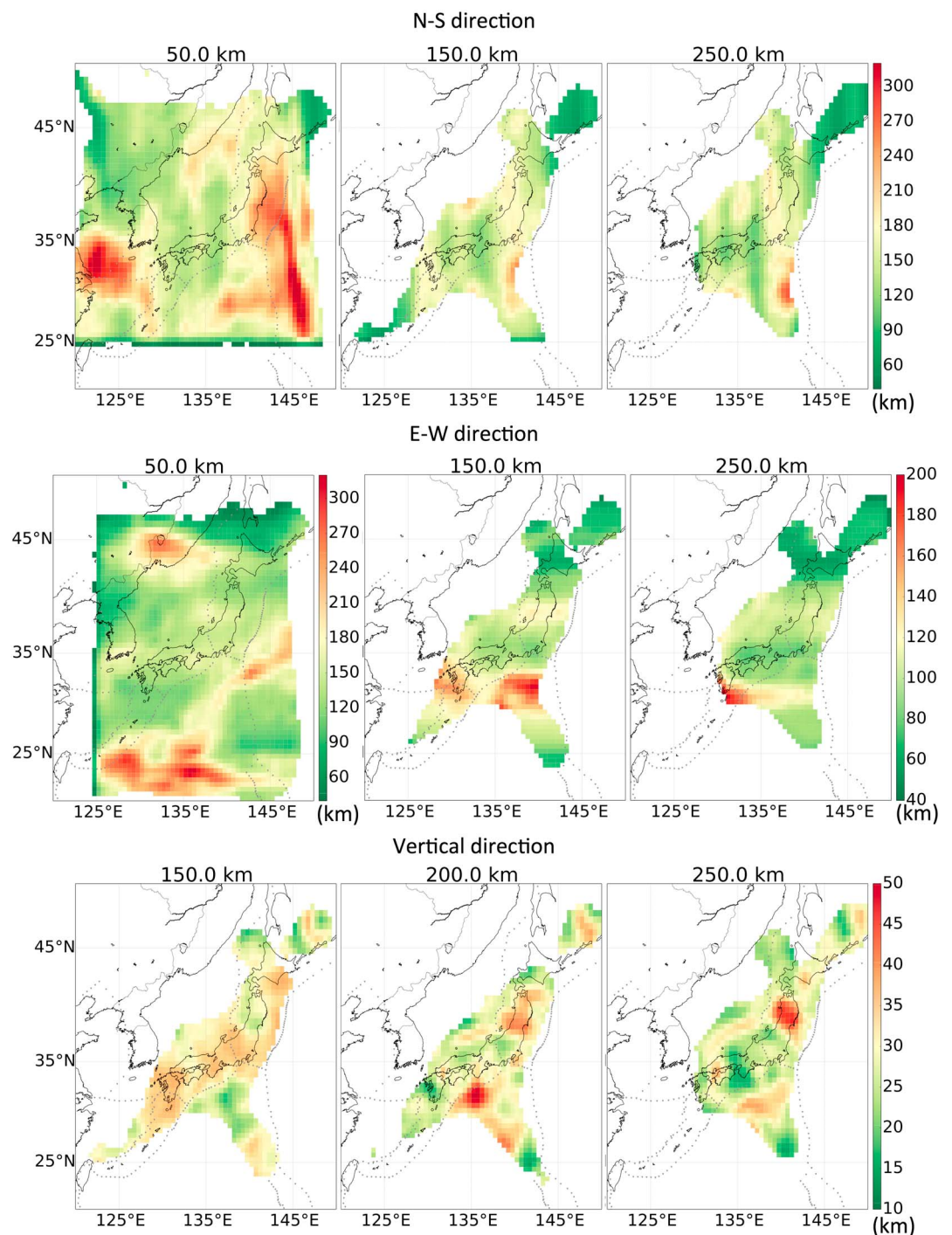


Figure 8. Position- and direction-dependent resolution length computed with the random probing technique of Fichtner and van Leeuwen [2015]. Resolution length in N-S direction is on average larger than in E-W direction due to the preferred N-S orientation of the event-receiver pairs. The incorporation of surface waves causes resolution length in the vertical direction to be around 3 times less than resolution length in the horizontal directions. The resolved volume shrinks with depth because body wave sensitivity covers less area than surface wave sensitivity at shallower depths. Dashed gray lines represent plate boundaries.

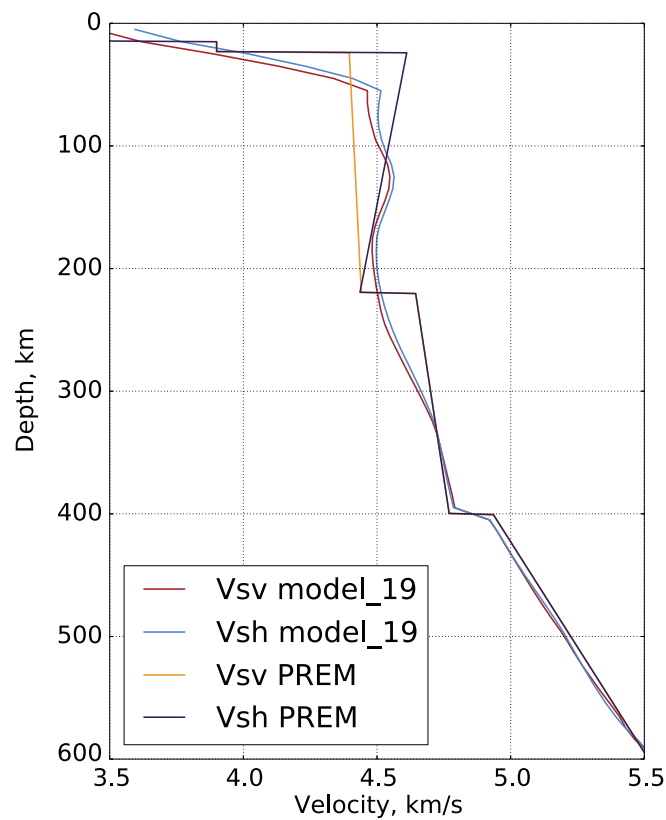


Figure 9. Lateral averages of SH and SV velocities in m_{19} at a frequency of 1 Hz. Isotropic S wave velocity was used as a reference to calculate velocity perturbations. For comparison, we also show SH and SV velocities for the radially symmetric Preliminary Reference Earth Model (PREM) [Dziwowski and Anderson, 1981].

Resolution length, defined as the half-width of the tomographic point-spread function, indicates the minimum separation distance needed to discern two hypothetical point-localized heterogeneities [e.g., Backus and Gilbert, 1968; Yanovskaya, 2000]. A resolution length of 100 km in E-W direction implies, for instance, that heterogeneities separated by more than 100 km in E-W direction can be recovered in the tomographic inversion in the form of two distinguishable features.

Resolution lengths themselves are spatially heterogeneous; an expected consequence of the nonuniform source-receiver distribution [e.g., Yanovskaya, 1997]. Furthermore, resolution varies significantly with direction, meaning that point-spread functions are strongly anisotropic. Around 100 km depth, resolution length in N-S direction approximately ranges between 150 and 250 km, and between 100 and 200 km in E-W direction. S velocity structure is generally better resolved in E-W direction than in N-S direction. This is due to the source-receiver distributions with an overall preferential N-S orientation that produces larger N-S than E-W smearing. Resolution length in vertical direction is shorter than in the horizontal directions, thanks to the incorporation of surface waves. Its mean value throughout the resolved volume is ~ 30 km. The resolution analysis shows that we can quantitatively interpret features located from the surface subduction of the Pacific plate in the east to the center of the Sea of Japan.

4.3. Model Results

4.3.1. Regional Lateral Averages

Figure 9 shows the laterally averaged SH and SV velocities of m_{19} , compared to those of the Preliminary Reference Earth Model (PREM) [Dziwowski and Anderson, 1981] at the reference frequency of 1 Hz. At depths below 300 km, the lateral averages of m_{19} and PREM differ by less than 1%. In contrast to PREM, we find two low-velocity zones, centered around 80 and 200 km depth, respectively. Within the uppermost mantle, average radial anisotropy in m_{19} is weak compared to PREM, mostly ranging below 2%. This is despite the strong variations of radial anisotropy that locally exceed $\pm 20\%$ within the upper 100 km of the model. More details on variations in anisotropy are provided in section 4.3.3.

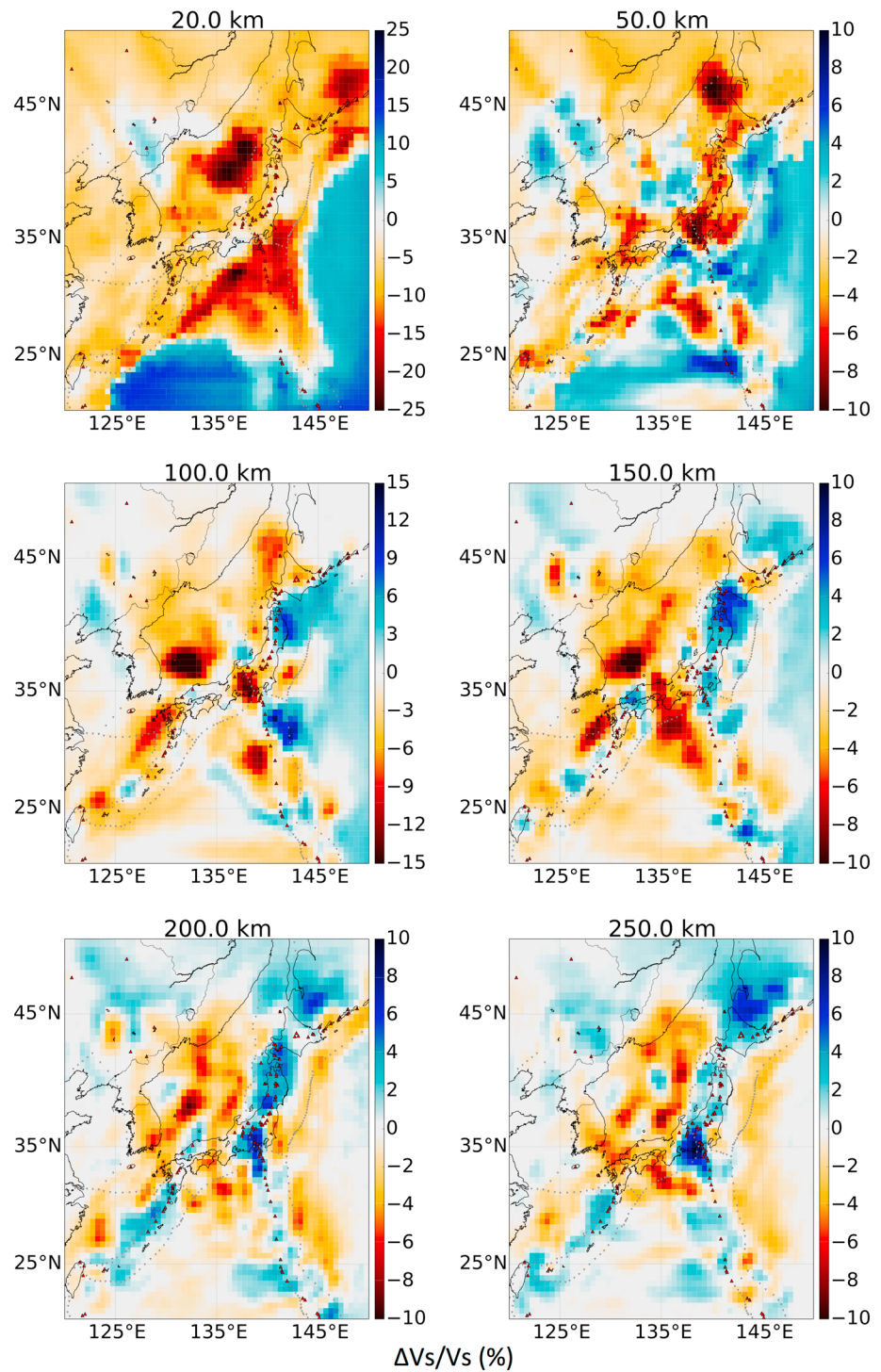


Figure 10. Depth slices of isotropic *S* velocity perturbations across the model domain. The Sea of Japan and the Shikoku basin are characterized by negative velocity perturbations, while positive velocity perturbations follow the Japan trench, the Izu-Bonin trench, the Nankai trough, and the Ryukyu trench. Note different color scales for the 20 km and 100 km depth slices. Dashed gray lines represent plate boundaries. Red triangles represent Holocene volcanoes [Siebert et al., 2010].

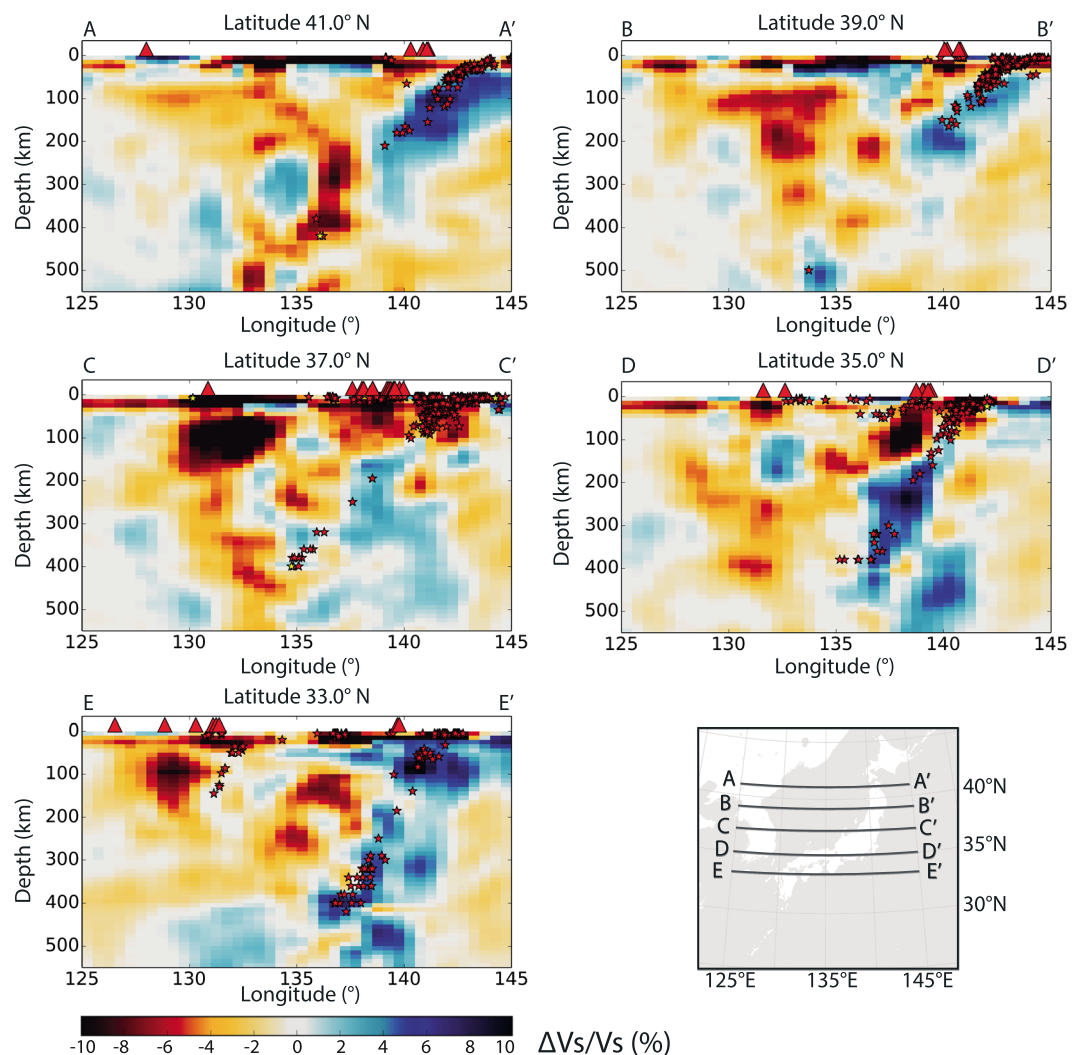


Figure 11. Cross section through the isotropic S velocity perturbations in the model domain. One can notice the slab steepening from the Japan trench in the north (AA') to the Izu-Bonin trench in the south. Negative velocity perturbations prevail in the upper mantle beneath the Sea of Japan (BB', CC'), and beneath the northeastern Japan (CC') and Izu-Bonin (DD') volcanic arcs. Red and yellow stars represent earthquakes since 1997 and earthquakes used in this study, respectively, within 1° of the slice. Red triangles represent Holocene volcanoes [Siebert et al., 2010].

4.3.2. Isotropic S Velocity Structure

In Figure 10, we present horizontal slices through the variations of isotropic S velocity, computed from the SH and SV velocities as $v_s = \sqrt{\frac{2}{3}v_{sv}^2 + \frac{1}{3}v_{sh}^2}$ [e.g., Babuška and Cara, 1991; Panning and Romanowicz, 2006]. Variations are with respect to the regional lateral average discussed in section 4.3.1. Vertical slices are shown in Figure 11.

We find high-velocity perturbations extending along the trenches of the subducted Pacific plate and advancing westward with increasing depth, which we associate with the Pacific slab. The slab is most clearly seen along the Japan and northern part of the Izu-Bonin trenches, extending to ~ 350 km depth, where resolution diminishes. The high-velocity feature along the southern part of the Izu-Bonin trench is weaker and more intermittent than along the Japan trench, which is partly due to limited ray coverage in this area.

The Sea of Japan is characterized by low S velocity from ~ 75 to ~ 250 km depth. This is in accord with recent S velocity results from ambient noise tomography [Zheng et al., 2011] and waveform tomography [Chen et al., 2015], as well as with low P velocities reported in a traveltimes study by Huang and Zhao [2006].

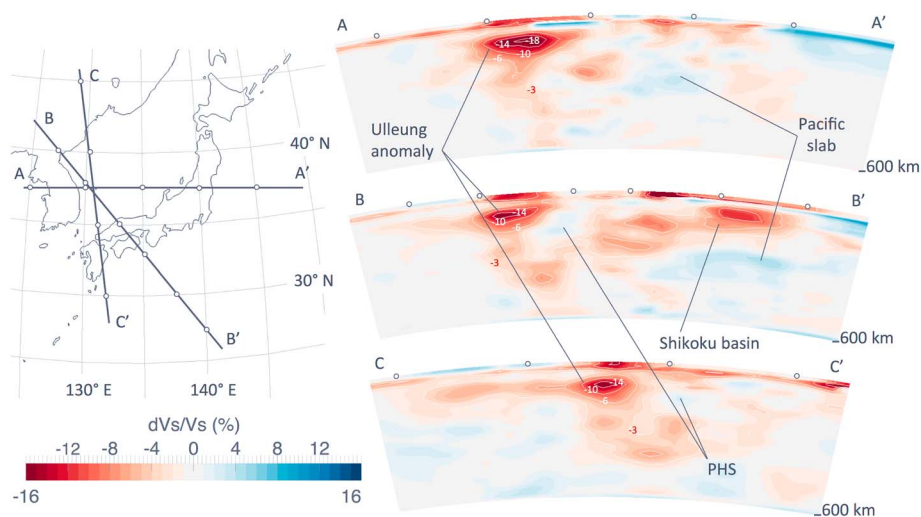


Figure 12. (right) Isotropic *S* velocity perturbation for the cross-sectional slices across the Ulleung volcano in the southwestern Sea of Japan with selected perturbation contours together with their (left) corresponding locations. The negative velocity perturbation related to the Ulleung anomaly originates at or above the Pacific slab below ~350 km depth (–3% contour seen in all the cross sections), rises vertically upward until the base of the Philippine Sea slab at ~200 km depth (BB'), circumvents it in the NW direction (BB'), and significantly strengthens in amplitude above the Philippine Sea slab. Also visible in BB' is the negative velocity perturbation related to the Shikoku basin.

A notable *S* velocity perturbation reaching –19.5%, is found off the east coast of South Korea, approximately beneath Ulleung Island. At 100 km depth, the –10% contour of this *Ulleung anomaly* is approximately 4° wide in the E-W direction (see also Figure 12). The strongest *S* velocity perturbations (–10% and lower) are located between 70 and 160 km depth (neglecting the crust), while a zone of –3% extends to the mantle transition zone (Figures 11 (CC') and 12), which suggests a deep origin of volcanism at Ulleung. The anomaly originates below 350 km depth, at or above the Pacific slab. It proceeds upward until it encounters the Philippine Sea slab, circumvents this positive velocity anomaly by deflecting to the NW direction, and reaches its largest amplitude in terms of negative velocity perturbation beneath the Ulleung basin (Figures 12 and 13). From the east, the anomaly might have some weaker contribution from the shallower part of the slab at around 200–300 km (Figures 11 (CC') and 12 (AA')). Our resolution analysis (see section 4.2) suggests that the majority of this negative velocity perturbation is at the boundary or within the well-constrained portion of the model.

Strong negative *S* velocity perturbations, as low as –11%, are distributed across central Honshu, where the Izu-Bonin arc meets the northeastern Japan arc. The low-velocity heterogeneity is confined to the upper ~125 km and can be most readily associated with the aforementioned volcanic arcs and active volcanoes,

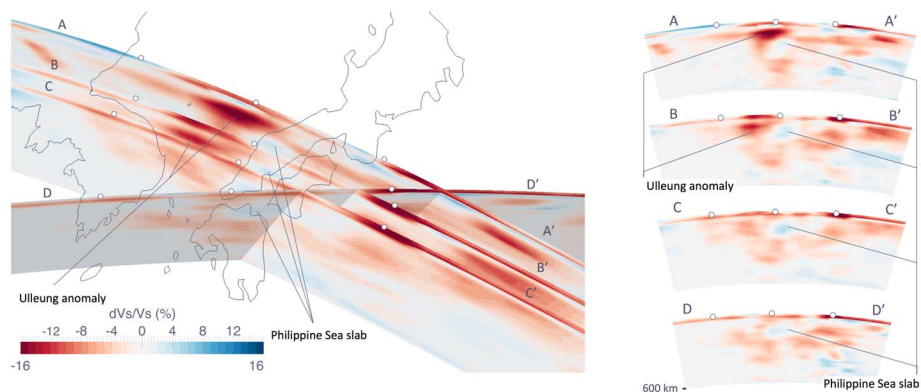


Figure 13. Isotropic *S* velocity perturbation for the cross-sectional slices across the Philippine Sea slab and the southwestern part of the Sea of Japan. For clarity, the slices are displayed separately to the right. Philippine Sea slab can be seen in all the slices down to ~200 km depth. The negative Ulleung basin perturbation is seen in slices AA' and BB'.

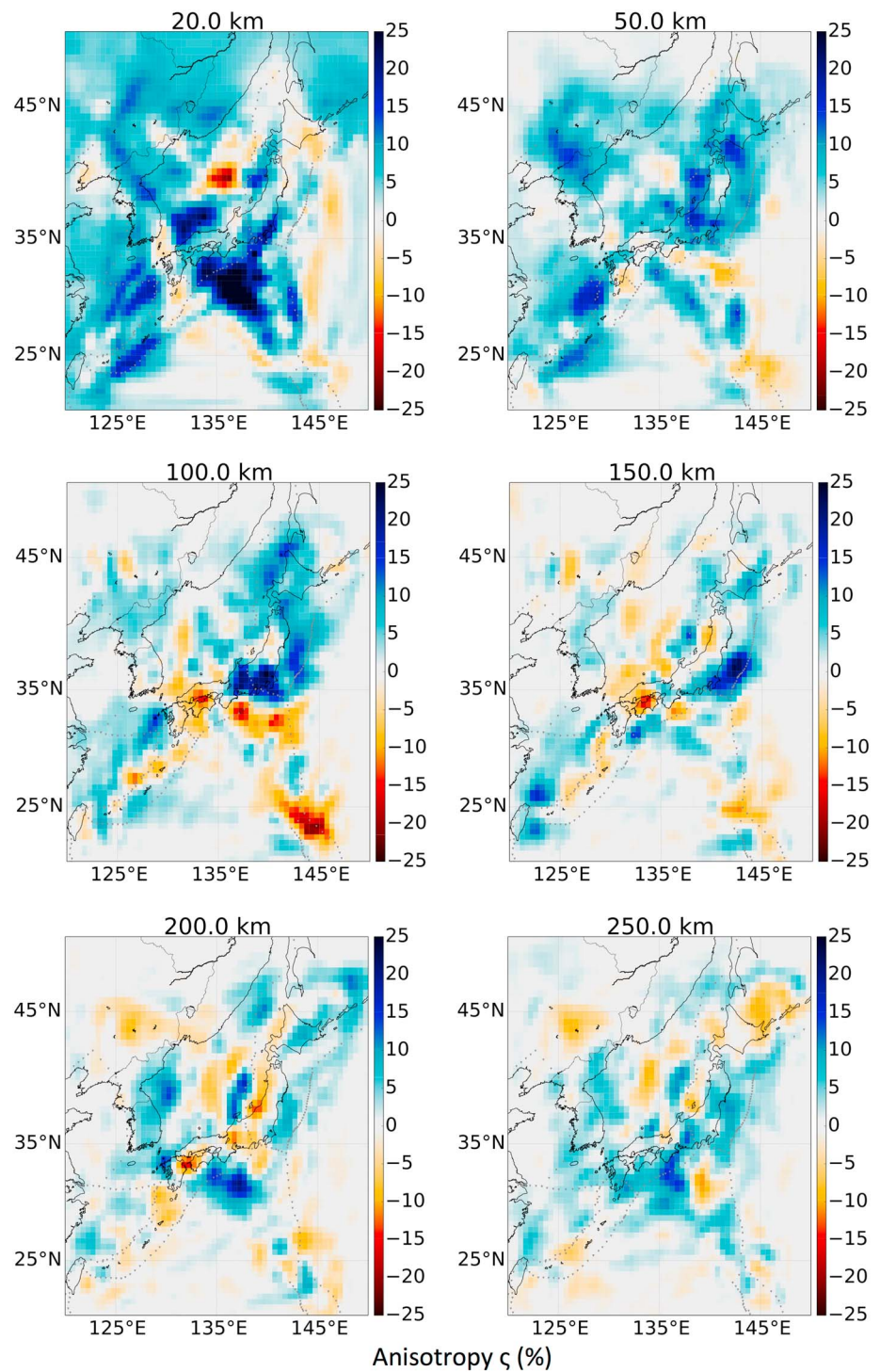


Figure 14. Radial anisotropy $\zeta = \frac{v_{sh} - v_{sv}}{v_s} \times 100\%$ for selected depths across the model domain. The model is dominated by positive anisotropy, meaning that $v_{sh} > v_{sv}$, which is expected in the uppermost mantle. From 100 to 200 km depth, patches of negative radial anisotropy are located roughly along the Nankai trough and the Izu-Bonin trench. An area of ζ reaching -25% exists beneath the Sea of Japan around 20 km depth.

such as Asamayama, Ontakesan, and Hakoneyama, located in the area. In the traveltime tomography by Matsubara *et al.* [2008], low S velocities reaching -8% are also found around the Izu peninsula at around 90–120 km depth.

The Shikoku basin, formed due to sea floor spreading in the northern Philippine Sea [Kobayashi *et al.*, 1995], is also characterized by lower than average S velocities (Figures 10 and 12). The low-velocity feature extends toward Shikoku Island and the Kii Peninsula and is visible most clearly at 150 km depth. A localized negative v_s anomaly below the eastern part of Shikoku Island and the Kii Peninsula was also found in traveltime tomography by Nakajima and Hasegawa [2007]. Our model shows this feature being connected to the Shikoku basin anomaly with ~ 150 km resolution in the N-S direction. The presence of a low-velocity anomaly in the northern part of the Philippine Sea was also confirmed in a recent traveltime study for the Japanese Islands [Wei *et al.*, 2015], and in large regional studies for East Asia, in P wave tomography [Wei *et al.*, 2012b; Huang and Zhao, 2006], and waveform inversion [Friederich, 2003].

4.3.3. Radial Anisotropy

Radial anisotropy, quantified as the relative difference between the SH and SV velocities, $\zeta = \frac{v_{sh}-v_{sv}}{v_s} \times 100\%$, varies strongly within the study region. As shown in Figure 14, ζ ranges between $\pm 25\%$ in the upper 150 km and then decreases gradually with increasing depth. While regions with $\zeta > 0$ prevail—in accord with most tomographic studies on larger scales [e.g., Ekström and Dziewonski, 1998; Panning and Romanowicz, 2006; Nettles and Dziewoński, 2008]—patches of pronounced negative radial anisotropy are clearly visible. From 100 to 200 km depth, a band of negative radial anisotropy roughly follows the Nankai trough and the Izu-Bonin trench. An isolated patch with ζ reaching -25% exists beneath the Sea of Japan around 20 km depth.

The relation of anisotropy to flow-induced lattice-preferred orientation of mantle minerals [Hess, 1964] makes it an interesting parameter for geodynamic studies. However, in addition to being related to flow, anisotropy is also affected by differential resolution, regularization of the tomographic inverse problem, pollution by more complex forms of anisotropy in the Earth that cannot be resolved, and the presence of equally unresolved subwavelength structure [e.g., Backus, 1962; Levshin and Ratnikova, 1984; Fichtner *et al.*, 2013; Capdeville *et al.*, 2015]. In the light of these difficulties, we deliberately abstain from a geologic interpretation of anisotropy, noting, however, that its presence is required to fit Love and Rayleigh wave data simultaneously.

5. Discussion

5.1. Physical Implication of Low Velocities in the Uppermost Mantle

For a quantitative interpretation of the observed anomalies, it is more diagnostic to work with absolute rather than relative velocities. A 19% negative anomaly in v_s at around 100 km corresponds to absolute v_s of 3.55 km/s. We computed the range of seismic velocities corresponding to the range of chemical compositions seen in mantle xenoliths [e.g., Afonso *et al.*, 2013] and basalts [e.g., Deschamps *et al.*, 2012], at feasible mantle temperatures using the thermodynamic modeling code *Perple_X* [Connolly, 2005]. The mineral anharmonic elastic velocities never reach as low as 3.55 km/s for these standard compositions. Temperature-dependent intrinsic anelasticity will reduce the velocities, especially in the presence of fluids [Behn *et al.*, 2009], but to attain S velocity of 3.55 km/s requires a quality factor (Q) of less than 40 (and likely closer to 10–20), which is not substantiated by surface wave observations [e.g., Dalton *et al.*, 2008; Yang *et al.*, 2007]. Partial melting, on the other hand, can reduce v_s by $\sim 7.9\%$ per percent melt [Hammond and Humphreys, 2000], and with the extensive range of rock compositions and temperatures that we modeled, we thus find that ~ 1 –2% melting is sufficient to generate a v_s of 3.55 km/s. Alternatively, Karato *et al.* [2015] demonstrated that “elastically accommodated grain boundary sliding” (EAGBS) can explain large negative S velocity anomalies at moderate temperatures, without melting. Using the formulation given in Karato *et al.* [2015], we find that EAGBS is indeed able to generate v_s as low as 3.55 km/s at 100 km. Neither melting nor EAGBS modifies Q at seismic frequencies, and thus, either of these mechanisms can explain the Ulleung anomaly.

5.2. Hypotheses for Ulleung Volcanism

Over the last several decades, a number of possible mechanisms were proposed to explain intraplate volcanism in northeastern China and the Sea of Japan. In the following section we present some of these mechanisms and proceed with an assessment of their respective compatibility with our tomographic model.

The extension of the mantle lithosphere during the back-arc opening allows for passive upwelling which can lead to (i) (buoyant) decompression melting [Ballmer *et al.*, 2015; Hernlund *et al.*, 2008]. Thus, decompression related to the opening of the Sea of Japan could have led to the low velocities in the uppermost mantle and

intraplate volcanism. A premature termination of the extensional regime due to the aforementioned migration of the Izu-Bonin arc might have left a remnant (ii) thermal perturbation, which had a negative effect on seismic velocities [Lee *et al.*, 1999]. (iii) A mantle plume beneath the Ulleung basin has also been suggested as a means to explain thicker than normal oceanic crust of the basin [Kim *et al.*, 1998].

(iv) A mobile “hot region” hypothesis was suggested to explain the opening of the Sea of Japan and scattered intraplate volcanism by Miyashiro [1986]. (v) Asthenospheric injection, unrelated to the slab subduction, has been proposed by Tatsumi *et al.* [1990]. A recent numerical modeling study aiming to dynamically restore the thermal state of the mantle showed that (vi) asthenospheric injection could have originated from beneath the Pacific slab, penetrated through the breaches of the subducting lithosphere, and subsequently led to the inhomogeneous spreading of the Sea of Japan [Ismail-Zadeh *et al.*, 2013].

A number of models relate intraplate volcanism and/or the opening of the Sea of Japan with the subduction of the Pacific slab. The fact that a subducting slab could induce convective circulation in the mantle wedge was recognized in the early 1970s [Sleep and Toksöz, 1971]. More recently, using numerical modeling, Faccenna *et al.* [2010] demonstrated that subduction could trigger (vii) a convective cell ahead of the slab in the upper mantle, leading to intraplate volcanism in the back-arc region. Zhao [2004] stressed the importance of the (viii) *big mantle wedge*, formed above the stagnant Pacific slab in the mantle transition zone. This and the subsequent studies [e.g., Zhao *et al.*, 2007] suggested that (ix) the deep dehydration of the slab together with the enhanced convective circulation in the wedge could cause intraplate volcanism in East Asia. In addition to the deep slab dehydration, other mechanisms were proposed which could trigger thermal or compositional instabilities that could then be entrained by the mantle flow. The numerical models by Motoki and Ballmer [2015], for example, showed that stagnant slabs in the mantle transition zone might become convectively unstable due to their upper part being thermally cooler and denser. As a result, (x) buoyancy-driven instabilities could rise from the underside of the stagnant slab [Motoki and Ballmer, 2015].

Laboratory studies have shown that mineral phases within the mantle transition zone, such as wadsleyite and ringwoodite, have much higher water solubility than minerals in the upper or lower mantle [Bercovici and Karato, 2003]. Numerical modeling suggested that as a result of a hydrated slab lingering in the transition zone, a hydrous layer of low density and viscosity could form at the top of the slab and lead to a small-scale convection and instabilities. Such instabilities were shown to merge together and form (xi) a “wet plume,” which could reach the base of the lithosphere and produce melt as a result of water-lowered solidus [Sheng *et al.*, 2016; Richard and Bercovici, 2009; Richard and Iwamori, 2010].

To begin with, we discard the mantle plume and hot region hypotheses (iii and iv). The deep-rooted mantle plume hypothesis lacks evidence for flood basalts, extensive volcanism, or a hot spot track in East Asia [Tang *et al.*, 2014], while the shallow-rooted ones might be linked to other mechanisms (e.g., lithosphere breakup) and thus are not a primary explanation for negative velocity perturbations [Courtillot *et al.*, 2003]. Accordingly, no plume beneath the Sea of Japan has been reported in mantle plume catalogs [e.g., Courtillot *et al.*, 2003; Montelli *et al.*, 2004a, 2006]. The hot region hypothesis spans over a large spatial and temporal domain. It has been proposed that the hot region had migrated from Australia 60 Ma ago to northern China at the present day [Miyashiro, 1986]. However, at limited spatial and temporal scales of the Ulleung basin such a hot region could be closely linked to the asthenospheric upwelling, which already exists in the list of considered mechanisms (v and vi).

While decompression related to the extension of the lithosphere (i) and thermal perturbation related to back-arc opening (ii) could have contributed to the anomaly at shallower depths, neither of the mechanisms could explain the deep origin from the top of the slab below 300 km. For the same reason, asthenospheric upwelling unrelated to the slab (v) is also unlikely. On the other hand, asthenospheric injection from beneath the slab (vi) could serve as an explanation for the deep origin of negative velocity perturbation. However, the limited spatial extent of our study region does not allow us to verify the existence of the gap in the Pacific slab. Besides, the origin of the injection would still remain to be resolved.

Upwellings from the tip of the subducting Pacific slab (vii) cannot really explain the volcanism at Ulleung as the slab seems to extend farther to the west beneath northeastern Asia [Lei and Zhao, 2005; Huang and Zhao, 2006; Li and van der Hilst, 2010; Wei *et al.*, 2015]. Furthermore, such a convective cell is expected to be most vigorous during the initial stages of subduction, fading away once the slab reaches the 660 km discontinuity [Faccenna *et al.*, 2010]. On the other hand, it is plausible that the subduction of the Philippine Sea plate could

have actually induced some sort of the convective cell around its tip in the southwestern part of the Sea of Japan (Figure 13). This could only be a contributing mechanism, as it cannot resolve the deep origin of the negative velocity perturbations.

We are left with hypotheses concerning the instabilities directly related to the slab at or before entering the mantle transition zone (ix–xi). Taking into account the fast rate of the subduction and the age of the Pacific slab, it is likely that fluids can be carried into the mantle transition zone and, as a result, play a role in the regional geodynamics. Intraplate volcanoes, found at the Lau spreading basin in a similar tectonic setting in the western Pacific, have been attributed to the deep dehydration processes enabled by the thermal structure of the old Tonga slab [Zhao *et al.*, 2007]. Low P velocity above the Pacific slab at ~ 400 km in southwestern Japan was also discovered by Zhao and Ohtani [2009], who invoked water, released from hydrous minerals, as a possible explanation. A similar deduction was made by Nakahigashi *et al.* [2015] to explain low velocities above the slab at 300–400 km depth beneath the Sea of Japan.

It is beyond the scope of this study to determine how and at which proportions water is accommodated in the mantle above the slab—whether it is hydrous phases, nominally anhydrous minerals, melt, or aqueous fluid phase—and whether it ascends upward by its own buoyancy or by the help of other transport mechanisms. However, it is known that the presence of water can reduce seismic velocities [Karato, 1995] as well as the solidus of the rock matrix [Thompson, 1992], which at particular p - T conditions could lead to melt generation. We think that some sort of instability is generated at the top of the slab either at or just before the mantle transition zone. The instability rises upward, aided by ambient mantle flow, such as a return flow within a (*big*) mantle wedge. The negative velocity perturbation reaches the lower part of the Philippine Sea slab and is forced to deflect and bend around it. During this stage, interactions with the overlying slab, e.g., slab melting, may be possible [Morris, 1995]. At depths shallower than 200 km, the anomaly strengthens in amplitude. If water was actually present within the upwelling material, p - T settings might be suitable for melt generation due to reduced solidus temperature.

5.3. Full-Waveform Inversion and Tomographic Resolution

While full-waveform inversion is computationally more expensive than most other tomographic techniques, it offers the advantage of being able to exploit complete seismic recordings for the benefit of improved tomographic resolution. In particular, by naturally inverting body *and* surface waves, full-waveform inversion combines the benefits of both data types. The use of surface waves prevents the vertical smearing that is typical for pure body wave tomographies in the upper mantle, which can be the source of false mantle plume sightings. Body waves provide additional lateral resolution that pure surface wave tomographies may not be able to achieve.

In this work, we paid special attention to quantitative resolution analysis that goes beyond qualitative and potentially misleading recovery tests [Lévéque *et al.*, 1993]. For this, we employed a random probing technique that yields the position- and direction-dependent width of the tomographic point-spread function [Fichtner and van Leeuwen, 2015], i.e., the resolution length (section 4.2). In addition to providing guidance in the tectonic interpretation, this is intended to facilitate quantitative comparison with future tomographic studies.

5.4. Low-Velocity Features

Improved resolution in full-waveform inversion is related not only to the natural joint inversion of different wave types but also to more accurate wave propagation physics compared to ray theory. The validity assumptions of ray theory break down when wave speed anomalies have large contrasts relative to the background medium and sizes similar to the wavelength. One facet of this breakdown is wavefront healing, first studied in detail by Wielandt [1987]. He noted that picked traveltimes decay with distance from the anomaly due to interference with diffracted waves, thereby leading to a bias in tomographic Earth models toward faster velocities. Montelli *et al.* [2004b] use a similar argument to explain velocity anomalies in finite-frequency tomography that are several percent larger than in ray tomography. In the most detailed analysis of seismic wavefront healing so far, Malcolm and Trampert [2011] note that the nature of wavefront healing depends on many factors, including the geometry of the anomaly and the technical details of how traveltimes are measured. They conclude that fast anomalies could even be perceived as being seismically slow.

Being based on numerical solutions of the seismic wave equation, full-waveform inversion properly accounts for wavefront healing, thus avoiding any bias that may be introduced by ray theory. This may explain the occurrence of unusually low velocity anomalies, such as the Ulleung anomaly that reaches -19.5% around

100 km depth (Figure 10 and section 4.3.2). In previous studies, we detected similar anomalies, for instance, beneath Iceland [Rickers *et al.*, 2013] and beneath the Valencia trough in the Mediterranean [Fichtner and Villaseñor, 2015].

5.5. Source Inversion

A major motivation of this work was to produce a 3-D regional model that can be used to constrain seismic sources with higher accuracy by (i) fully accounting for crustal and upper mantle heterogeneity and (ii) exploiting complete seismograms. The use of 3-D instead of 1-D models has repeatedly been shown to yield more reliable point-source locations and moment tensor solutions [e.g., Hingee *et al.*, 2011; Zhu *et al.*, 2015], which is critical for near-real-time applications such as earthquake and tsunami warning. Furthermore, we expect our model to contribute to the quality of finite-source inversions in the Japan region. The latter still show great variability that is often beyond the uncertainties quantified by individual authors [e.g., Shao *et al.*, 2011; Hayes, 2011; Lay *et al.*, 2011; Ammon *et al.*, 2011; Yamazaki *et al.*, 2011; Wei *et al.*, 2012a].

6. Conclusions

We presented a full seismic waveform inversion for the crust and upper mantle beneath the Japanese Islands region. Our method is based on (i) GPU-accelerated spectral-element simulations of seismic wave propagation in anisotropic Earth models with attenuation [Gokhberg and Fichtner, 2016], (ii) adjoint techniques for the computation of sensitivity kernels, and (iii) the nonlinear minimization of time-frequency misfits [Fichtner *et al.*, 2008] between observed and synthetic three-component waveforms from 58 events recorded at 165 stations. Full-waveform inversion accurately accounts for the physics of wave propagation in 3-D heterogeneous media, avoids crustal corrections, naturally uses correct finite-frequency kernels, and jointly inverts both body and surface wave data.

Our model explains complete seismic waveforms of events not used in the inversion in the period range from 20 to 80 s. This indicates that the iterative minimization was stopped early enough to avoid overfitting and that our model may be used in the future to improve (finite) earthquake source inversion in the region. Quantitative resolution analysis based on random probing of the Hessian [Fichtner and van Leeuwen, 2015] shows that resolution lengths within the well-covered areas are around 150 km in the horizontal and around 30 km in the vertical directions. These values vary as a function of azimuthal and absolute coverage.

In addition to the high-velocity signatures of the well-studied Pacific and Philippine Sea slabs, our model reveals a pronounced low-velocity anomaly beneath the volcanic island of Ulleung in the Sea of Japan, reaching -19% around 100 km depth. Located within the well-resolved portion of the model, the Ulleung anomaly can be seen to originate at or above the Pacific slab. From there it rises nearly vertically upward to the base of the Philippine Sea slab at ~ 200 km depth, which it circumvents in NW direction, before rising farther into the uppermost mantle. There it strengthens significantly in terms of the S velocity anomaly. Based on our tomographic model and geodynamic arguments, we hypothesize that the Ulleung anomaly originates as a result of fluid-related instabilities within or above the mantle transition zone, which are facilitated by the age and fast subduction of the Pacific slab.

By avoiding the high-frequency limitations of ray theory, typically characterized by the inability to resolve structure at comparable sizes to the wavelength or in areas of high velocity contrast, we avoid a bias toward higher velocities [e.g., Wielandt, 1987; Montelli *et al.*, 2004b; Malcolm and Trampert, 2011; Rickers *et al.*, 2012]. We suggest that our use of the full seismic waveform combined with advanced wavefield modeling and inversion allows us to detect unusually low S velocity anomaly beneath the Ulleung volcanic island, which ray theory may have otherwise obscured in past investigations.

References

- Afonso, J. C., J. Fullea, W. L. Griffin, Y. Yang, A. G. Jones, J. A. D. Connolly, and S. Y. O'Reilly (2013), 3-D multiobservable probabilistic inversion for the compositional and thermal structure of the lithosphere and upper mantle. I: A priori petrological information and geophysical observables, *J. Geophys. Res. Solid Earth*, *118*, 2586–2617, doi:10.1002/jgrb.50124.
- Ammon, C. J., T. Lay, H. Kanamori, and M. Cleveland (2011), A rupture model of the 2011 off the Pacific coast of Tohoku earthquake, *Earth planet. Space*, *63*, 693–696.
- Archuleta, R. J. (1984), A faulting model for the 1979 Imperial Valley earthquake, *J. Geophys. Res.*, *89*, 4559–4585.
- Babuška, V., and M. Cara (1991), *Seismic Anisotropy in the Earth*, Kluwer Acad., Dordrecht, Boston, London.
- Backus, G. E. (1962), Long-wave elastic anisotropy produced by horizontal layering, *J. Geophys. Res.*, *67*, 4427–4440.
- Backus, G. E., and F. Gilbert (1968), The resolving power of gross Earth data, *Geophys. J. Roy. Astr. Soc.*, *16*, 169–205.

Acknowledgments

The authors would like to thank Maxim Ballmer, Rob Govers, Wim Spakman, and Ylona van Dinther for useful discussions and brainstorming sessions as well as Sung-Joon Chang for technical assistance in retrieving data from the Korea National Seismograph Network. We also thank the Editors and the two anonymous reviewers for their constructive comments, which helped to improve the manuscript. This research was supported by the Swiss National Supercomputing Center (CSCS) in the form of the GeoScale and CH1 projects, by the Swiss National Science Foundation (SNF) under grant 200021_149143, and by the Netherlands Organization for Scientific Research (VIDI grant 864.11.008). All seismic waveform data used in this study are freely available from the Full Range Seismograph Network of Japan (F-Net, <http://www.fnet.bosai.go.jp/>), the Broadband Array in Taiwan for Seismology (BATS, <http://bats.earth.sinica.edu.tw/>), the Korea National Seismograph Network (<http://www.kma.go.kr/weather/earthquake/internationalist.jsp>), and the China National Seismic Network, the New China Digital Seismograph Network, the Global Seismograph Network, and the Korean Seismic Network, made available by the IRIS Data Management Center (<http://ds.iris.edu/ds/nodes/dmc/>).

- Ballmer, M., P. van Keken, and G. Ito (2015), Hotspots, large igneous provinces, and melting anomalies, in *Treatise on Geophysics*, vol. 7, edited by G. Schubert et al., pp. 371–435, Elsevier, Amsterdam.
- Bamberger, A., G. Chavent, C. Hemons, and P. Lailly (1982), Inversion of normal incidence seismograms, *Geophysics*, *47*, 757–770.
- Behn, M. D., G. Hirth, and J. E. II (2009), Implications of grain-size evolution on the seismic structure of the oceanic upper mantle, *Earth Planet. Sci. Lett.*, *282*, 178–189.
- Bercovici, D., and S. Karato (2003), Whole-mantle convection and the transition-zone water filter, *Nature*, *425*, 39–44.
- Bird, P. (2003), An updated digital model of plate boundaries, *Geochem. Geophys. Geosys.*, *4*, 1027–1079.
- Bozdağ, E., and J. Trampert (2008), On crustal corrections in surface wave tomography, *Geophys. J. Int.*, *172*, 1066–1082.
- Bunks, C., F. M. Saleck, S. Zaleski, and G. Chavent (1995), Multiscale seismic waveform inversion, *Geophysics*, *60*, 1457–1473.
- Capdeville, Y., M. Zhao, and P. Cupillard (2015), Fast Fourier homogenization for elastic wave propagation in complex media, *Wave Motion*, *50*, 170–186.
- Cerveny, V. (2001), *Seismic Ray Theory*, Cambridge Univ. Press, Cambridge.
- Chen, M., F. Niu, Q. Liu, J. Tromp, and X. Zheng (2015), Multi-parameter adjoint tomography of the crust and upper mantle beneath East Asia—Part I: Model construction and comparisons, *J. Geophys. Res.*, *120*, 1762–1786.
- Chen, P., L. Zhao, and T. H. Jordan (2007), Full 3D tomography for the crustal structure of the Los Angeles region, *Bull. Seismol. Soc. Am.*, *97*, 1094–1120.
- Colli, L., A. Fichtner, and H.-P. Bunge (2013), Full waveform tomography of the upper mantle in the South Atlantic region: Imaging westward fluxing shallow asthenosphere?, *Tectonophysics*, *604*, 26–40.
- Connolly, J. (2005), Computation of phase equilibria by linear programming: A tool for geodynamic modelling and its application to subduction zone decarbonation, *Earth Planet. Sci. Lett.*, *236*, 524–541.
- Cotton, F., and M. Campillo (1995), Frequency-domain inversion of strong ground motions: Application to the 1992 Landers earthquake, *J. Geophys. Res.*, *100*, 3961–3975.
- Courtillot, V., A. Davaille, J. Besse, and J. Stock (2003), Three distinct types of hotspots in the Earth's mantle, *Earth Planet. Sci. Lett.*, *205*(3–4), 295–308.
- Dalton, C. A., G. Ekström, and A. M. Dziewonski (2008), The global attenuation structure of the upper mantle, *J. Geophys. Res.*, *113*, B09303, doi:10.1029/2007JB005429.
- Deschamps, F., L. Cobden, and P. J. Tackley (2012), The primitive nature of large low shear-wave velocity provinces, *Earth Planet. Sci. Lett.*, *349–350*, 198–208.
- Diaz-Steptoe, H. (2013), Full seismic waveform tomography of the Japan region using adjoint methods, Master thesis, Utrecht Univ., Utrecht, Netherlands.
- Durek, J. J., and G. Ekström (1996), A radial model of anelasticity consistent with long-period surface wave attenuation, *Bull. Seismol. Soc. Am.*, *86*, 144–158.
- Dziewoński, A. M., and D. L. Anderson (1981), Preliminary reference Earth model, *Phys. Earth Planet. Inter.*, *25*, 297–356.
- Ekström, G., and A. M. Dziewonski (1998), The unique anisotropy of the Pacific upper mantle, *Nature*, *394*, 168–172.
- Ekström, G., M. Nettles, and A. M. Dziewonski (2012), The global CMT project 2004–2010: Centroid moment tensors for 13,017 earthquakes, *Phys. Earth Planet. Inter.*, *200–201*, 1–9.
- Faccenna, C., T. W. Becker, S. Lallemand, Y. Lagabrielle, F. Funiciello, and C. Piromallo (2010), Subduction-triggered magmatic pulses: A new class of plumes?, *Earth Planet. Sci. Lett.*, *299*, 54–68.
- Faccioli, E., F. Maggio, A. Quarteroni, and A. Tagliani (1996), Spectral-domain decomposition methods for the solution of acoustic and elastic wave equations, *Geophysics*, *61*:4, 1160–1174.
- Fichtner, A. (2010), *Full Seismic Waveform Modelling and Inversion*, Springer, Heidelberg.
- Fichtner, A., and H. Igel (2008), Efficient numerical surface wave propagation through the optimization of discrete crustal models—A technique based on non-linear dispersion curve matching (DCM), *Geophys. J. Int.*, *173*, 519–533.
- Fichtner, A., and J. Trampert (2011), Hessian kernels of seismic data functionals based upon adjoint techniques, *Geophys. J. Int.*, *185*, 775–798.
- Fichtner, A., and T. van Leeuwen (2015), Resolution analysis by random probing, *J. Geophys. Res.*, *120*, 5549–5573, doi:10.1002/2015JB012106.
- Fichtner, A., and A. Villaseñor (2015), Crust and upper mantle of the western Mediterranean—Constraints from full-waveform inversion, *Earth Planet. Sci. Lett.*, *428*, 52–62.
- Fichtner, A., H.-P. Bunge, and H. Igel (2006), The adjoint method in seismology—I. Theory, *Phys. Earth Planet. Inter.*, *157*, 86–104.
- Fichtner, A., B. L. N. Kennett, H. Igel, and H.-P. Bunge (2008), Theoretical background for continental- and global-scale full-waveform inversion in the time-frequency domain, *Geophys. J. Int.*, *175*, 665–685.
- Fichtner, A., B. L. N. Kennett, H. Igel, and H.-P. Bunge (2009a), Full seismic waveform tomography for upper-mantle structure in the Australasian region using adjoint methods, *Geophys. J. Int.*, *179*, 1703–1725.
- Fichtner, A., B. L. N. Kennett, H. Igel, and H.-P. Bunge (2009b), Spectral-element simulation and inversion of seismic waves in a spherical section of the Earth, *J. Numer. Anal. Ind. Appl. Math.*, *4*, 11–22.
- Fichtner, A., B. L. N. Kennett, and J. Trampert (2013), Separating intrinsic and apparent anisotropy, *Phys. Earth Planet. Inter.*, *219*, 11–20.
- Friederich, W. (2003), The S-velocity structure of the East Asian mantle from inversion of shear and surface waveforms, *Geophys. J. Int.*, *153*, 88–102.
- Fukuyama, E., M. Ishida, D. Dreger, and H. Kawai (1998), Automated seismic moment tensor determination by using on-line broadband seismic waveforms [in Japanese with English abstract], *J. Seismol. Soc. Jpn.*, *51*, 149–156.
- Gallovic, F., W. Imperatori, and P. M. Mai (2015), Effects of three-dimensional crustal structure and smoothing constraint on earthquake slip inversions: Case study of the M_w 6.3 2009 L'Aquila earthquake, *J. Geophys. Res. Solid Earth*, *120*, 428–449, doi:10.1002/2014JB011650.
- Gokhberg, A., and A. Fichtner (2016), Full-waveform inversion on heterogeneous HPC systems, *Comp. Geosci.*, *89*, 260–268.
- Graves, R. W., and D. J. Wald (2001), Resolution analysis of finite fault source inversion using one- and three-dimensional Green's functions—1: Strong motions, *J. Geophys. Res.*, *106*, 8745–8766.
- Hall, R. (2002), Cenozoic geological and plate tectonic evolution of SE Asia and the SW Pacific: Computer-based reconstructions, model and animations, *J. Asian Earth Sci.*, *20*, 353–431.
- Hammond, W. C., and E. D. Humphreys (2000), Upper mantle seismic wave velocity: Effects of realistic partial melt geometries, *J. Geophys. Res.*, *105*(B5), 10,975–10,986.
- Hayes, G. (2011), Rapid source characterization of the 03-11-2011 M_w 9.0 off the Pacific coast of Tohoku earthquake, *Earth Planet. Space*, *63*, 529–534.

- Hernlund, J., P. Tackley, and D. Stevenson (2008), Buoyant melting instabilities beneath extending lithosphere: 1. Numerical models, *J. Geophys. Res.*, *113*, B04405, doi:10.1029/2006JB004862.
- Hess, H. H. (1964), Seismic anisotropy of the uppermost mantle under oceans, *Nature*, *203*, 629–631.
- Hingee, M., H. Tkalčić, A. Fichtner, and M. Sambridge (2011), Seismic moment tensor inversion using a 3-D structural model: Applications for the Australian region, *Geophys. J. Int.*, *184*, 949–964.
- Huang, J., and D. Zhao (2006), High-resolution mantle tomography of China and surrounding regions, *J. Geophys. Res.*, *111*, B09305, doi:10.1029/2005JB004066.
- Igel, H., H. Dijkpessie, and A. Tarantola (1996), Waveform inversion of marine reflection seismograms for P impedance and Poisson's ratio, *Geophys. J. Int.*, *124*, 363–371.
- Ingle, J. C. (1992), Subsidence of the Japan Sea: Stratigraphic evidence from ODP sites and onshore sections, *Proc. Ocean Drill. Program Part B Sci. Results*, *127/128*, 1197–1218.
- Ismail-Zadeh, A., S. Honda, and S. Tsepelev (2013), Linking mantle upwelling with the lithosphere descent and the Japan Sea evolution: A hypothesis, *Sci. Rep.*, *3*, 1137, doi:10.1038/srep01137.
- Itoh, Y. (1988), Differential rotation of the eastern part of southwest Japan inferred from paleomagnetism of Cretaceous and Neogene rocks, *J. Geophys. Res.*, *93*(B4), 3401–3411.
- Jolivet, L., K. Tamaki, and M. Fournier (1994), Japan Sea, opening history and mechanism: A synthesis, *J. Geophys. Res.*, *99*(B11), 22,237–22,259.
- Karato, S.-I. (1995), Effects of water on seismic wave velocities in the upper mantle, *Proc. Japan Acad.*, *71*, 61–66.
- Karato, S.-I., T. Ologboji, and J. Park (2015), Mechanisms and geologic significance of the mid-lithosphere discontinuity in the continents, *Nat. Geosci.*, *8*, 509–514, doi:10.1038/ngeo2462.
- Kim, H.-J., S.-J. Han, G. H. Lee, and S. Huh (1998), Seismic study of the Ulleung Basin crust and its implications for the opening of the East Sea (Japan Sea), *Mar. Geophys. Res.*, *20*, 219–237.
- Kim, K. H., T. Tanaka, K. Nagao, and S. K. Jang (1999), Nd and Sr isotopes and K-Ar ages of the Ulreungdo alkali volcanic rocks in the East Sea, South Korea, *Geochem. J.*, *33*, 317–341.
- Kobayashi, K., S. Kasuga, and K. Okino (1995), Shikoku Basin and its margins, in *Backarc Basins*, edited by K. Kobayashi, S. Kasuga, and K. Okino, pp. 381–405, Springer, New York.
- Komatitsch, D., and J. Tromp (2002), Spectral-element simulations of global seismic wave propagation. Part I: Validation, *Geophys. J. Int.*, *149*, 390–412.
- Komatitsch, D., and J. P. Vilotte (1998), The spectral element method: An effective tool to simulate the seismic response of 2D and 3D geological structures, *Bull. Seismol. Soc. Am.*, *88*, 368–392.
- Krischer, L., A. Fichtner, S. Žukauskaitė, and H. Igel (2015), Large-scale seismic inversion framework, *Seismol. Res. Lett.*, *86*, 1198–1207.
- Lay, T., C. J. Ammon, H. Kanamori, L. Xue, and M. J. Kim (2011), Possible large near-trench slip during the 2011 M_w 9.0 off the Pacific coast of Tohoku earthquake, *Earth planet. Space*, *63*, 687–692.
- Lee, G. H., H. J. Kim, M. C. Suh, and J. K. Hong (1999), Crustal structure, volcanism, and opening mode of the Ulleung Basin, East Sea (Sea of Japan), *Tectonophysics*, *308*, 503–525.
- Lei, J., and D. Zhao (2005), P -wave tomography and origin of the Changbai intraplate volcano in Northeast Asia, *Tectonophysics*, *397*(3–4), 281–295, doi:10.1016/j.tecto.2004.12.009.
- Lévêque, J. J., L. Rivera, and G. Wittlinger (1993), On the use of the checkerboard test to assess the resolution of tomographic inversions, *Geophys. J. Int.*, *115*, 313–318.
- Levshin, A., and L. Ratnikova (1984), Apparent anisotropy in inhomogeneous media, *Geophys. J. R. Astron. Soc.*, *76*, 65–69.
- Li, C., and R. D. van der Hilst (2010), Structure of the upper mantle and transition zone beneath Southeast Asia from traveltimes tomography, *J. Geophys. Res.*, *115*(B7), B07308, doi:10.1029/2009JB006882.
- Liu, Q., and J. Tromp (2008), Finite-frequency sensitivity kernels for global seismic wave propagation based upon adjoint methods, *Geophys. J. Int.*, *174*, 265–286.
- Mai, P. M., and K. K. S. Thingbaijam (2014), SRCMOD: An online database of finite-fault rupture models, *Seismol. Res. Lett.*, *85*, 1348–1357.
- Malcolm, A. E., and J. Trampert (2011), Tomographic errors from wave front healing: More than just a fast bias, *Geophys. J. Int.*, *185*, 385–402.
- Matsubara, M., K. Obara, and K. Kasahara (2008), Three-dimensional P - and S -wave velocity structures beneath the Japan Islands obtained by high-density seismic stations by seismic tomography, *Tectonophysics*, *454*, 86–103.
- Miyashiro, A. (1986), Hot regions and the origin of marginal basins in the western Pacific, *Tectonophysics*, *122*, 195–216.
- Montelli, R., G. Nolet, F. Dahlen, G. Masters, E. Engdahl, and S. Hung (2004a), Finite-frequency tomography reveals a variety of mantle plumes, *Science*, *303*, 338–343.
- Montelli, R., G. Nolet, G. Masters, F. A. Dahlen, and S.-H. Hung (2004b), Global P and PP traveltimes tomography: Ray versus waves, *Geophys. J. Int.*, *158*, 637–654.
- Montelli, R., G. Nolet, F. Dahlen, and G. Masters (2006), A catalogue of deep mantle plumes: New results from finite-frequency tomography, *Geochem. Geophys. Geosyst.*, *7*, Q11007, doi:10.1029/2006GC001248.
- Morris, P. (1995), Slab melting as an explanation of Quaternary volcanism and aseismicity in southwest Japan, *Geology*, *23*(5), 395–398.
- Motoki, M., and M. Ballmer (2015), Intraplate volcanism due to convective instability of stagnant slabs in the mantle transition zone, *Geochem. Geophys. Geosyst.*, *16*, 538–551, doi:10.1002/2014GC005608.
- Nakahigashi, K., M. Shinohara, T. Yamada, K. Uehira, S. Sakai, K. Mochizuki, H. Shiobara, and T. Kanazawa (2015), Deep slab dehydration and large-scale upwelling flow in the upper mantle beneath the Japan Sea, *J. Geophys. Res. Solid Earth*, *120*, 3278–3292, doi:10.1002/2014JB011781.
- Nakajima, J., and A. Hasegawa (2007), Tomographic evidence for the mantle upwelling beneath southwestern Japan and its implications for arc magmatism, *Earth Planet. Sci. Lett.*, *254*(1–2), 90–105.
- Nettles, M., and A. M. Dziewoński (2008), Radially anisotropic shear velocity structure of the upper mantle globally and beneath North America, *J. Geophys. Res.*, *113*, B02303, doi:10.1029/2006JB004819.
- Panning, M., and B. Romanowicz (2006), A three-dimensional radially anisotropic model of shear velocity in the whole mantle, *Geophys. J. Int.*, *167*, 361–379.
- Pratt, R. G. (1999), Seismic waveform inversion in the frequency domain. Part 1: Theory and verification in a physical scale model, *Geophysics*, *64*, 888–901.
- Priolo, E., J. M. Carcione, and G. Seriani (1994), Numerical simulation of interface waves by high-order spectral modeling techniques, *J. Acoust. Soc. Am.*, *95*(2), 681–693.
- Razafindrakoto, H. N. T., and P. M. Mai (2014), Uncertainty in earthquake source imaging due to variations in source time function and Earth structure, *Bull. Seismol. Soc. Am.*, *104*, 855–874.

- Richard, G., and D. Bercovici (2009), Water-induced convection in the Earth's mantle transition zone, *J. Geophys. Res.*, *114*, B01205, doi:10.1029/2008JB005734.
- Richard, G., and H. Iwamori (2010), Stagnant slab, wet plumes and Cenozoic volcanism in East Asia, *Phys. Earth Planet. Inter.*, *183*, 280–287.
- Rickers, F., A. Fichtner, and J. Trampert (2012), Imaging mantle plumes with instantaneous phase measurements of diffracted waves, *Geophys. J. Int.*, *190*, 650–664.
- Rickers, F., A. Fichtner, and J. Trampert (2013), The Iceland–Jan Mayen plume system and its impact on mantle dynamics in the North Atlantic region: Evidence from full-waveform inversion, *Earth Planet. Sci. Lett.*, *367*, 39–51.
- Santosa, F., and W. W. Symes (1988), Computation of the Hessian for least-squares solutions of inverse problems of reflection seismology, *Inverse Prob.*, *4*, 211–233.
- Seriani, G., and E. Priolo (1994), Spectral element method for acoustic wave simulation in heterogeneous media, *Finite Elem. Anal. Des.*, *16*, 337–348.
- Shao, G., X. Li, C. Ji, and T. Maeda (2011), Focal mechanism and slip history of the 2011 M_w 9.1 off the Pacific coast of Tohoku earthquake, constrained with teleseismic body and surface waves, *Earth Planet. Space*, *63*, 559–564.
- Sheng, J., J. Liao, and T. Gerya (2016), Numerical modeling of deep oceanic slab dehydration: Implications for the possible origin of far field intra-continental volcanoes in northeastern China, *J. Asian Earth Sci.*, *117*, 328–336.
- Siebert, L., T. Simkin, and P. Kimberley (2010), *Volcanoes of the World*, 3rd edn., p. 551, Univ. of Calif. Press, Berkeley.
- Sleep, N., and N. Toksöz (1971), Evolution of marginal basins, *Nature*, *233*, 548–550.
- Taira, A. (2001), Tectonic evolution of the Japanese Island arc system, *Annu. Rev. Earth Planet. Sci.*, *29*, 109–134.
- Tang, Y., M. Obayashi, F. Niu, S. Grand, Y. Chen, H. Kawakatsu, S. Tanaka, J. Ning, and J. Ni (2014), Changbaishan volcanism in northeast China linked to subduction-induced mantle upwelling, *Nat. Geosci.*, *7*, 470–475.
- Tape, C., Q. Liu, A. Maggi, and J. Tromp (2010), Seismic tomography of the southern California crust based upon spectral-element and adjoint methods, *Geophys. J. Int.*, *180*, 433–462.
- Tarantola, A. (1988), Theoretical background for the inversion of seismic waveforms, including elasticity and attenuation, *Pure Appl. Geophys.*, *128*, 365–399.
- Tatsumi, Y., S. Maruyama, and S. Nohda (1990), Mechanism of backarc opening in the Japan Sea: Role of asthenospheric injection, *Tectonophysics*, *181*, 299–306.
- Thompson, A. (1992), Water in the Earth's upper mantle, *Nature*, *358*, 295–302.
- Tromp, J., C. Tape, and Q. Liu (2005), Seismic tomography, adjoint methods, time reversal and banana-doughnut kernels, *Geophys. J. Int.*, *160*, 195–216.
- Wakita, K. (2013), Geology and tectonics of Japanese Islands: A review—The key to understanding the geology of Asia, *J. Asian Earth Sci.*, *72*, 75–87.
- Wei, S., R. W. Graves, D. Helmberger, J. P. Avouac, and J. Jiang (2012a), Source of shaking and flooding during the Tohoku-Oki earthquake: A mixture of rupture styles, *Earth Planet. Sci. Lett.*, *333*, 91–100.
- Wei, W., J. Xu, D. Zhao, and Y. Shi (2012b), East Asia mantle tomography: New insight into plate subduction and intraplate volcanism, *J. Asian Earth Sci.*, *60*, 88–103.
- Wei, W., D. Zhao, J. Xu, F. Wei, and G. Liu (2015), *P* and *S* wave tomography and anisotropy in Northwest Pacific and East Asia: Constraints on stagnant slab and intraplate volcanism, *J. Geophys. Res. Solid Earth*, *120*(3), 1642–1666, doi:10.1002/2014JB011254.
- Wielandt, E. (1987), On the validity of the ray approximation for the interpreting delay times, in *Seismic Tomography*, pp. 85–98, Springer, Netherlands.
- Yamazaki, Y., T. Lay, K. F. Cheung, H. Yue, and H. Kanamori (2011), Modeling near-field tsunami observations to improve finite-fault slip models for the 11 March 2011 Tohoku earthquake, *Geophys. Res. Lett.*, *38*, L00G15, doi:10.1029/2011GL049130.
- Yang, Y., D. W. Forsyth, and D. S. Weeraratne (2007), Seismic attenuation near the East Pacific Rise and the origin of the low-velocity zone, *Earth Planet. Sci. Lett.*, *268*, 260–268.
- Yanovskaya, T. B., (1997), Resolution estimation in the problems of seismic ray tomography, *Izv. Phys. Solid Earth*, *33*, 76–80.
- Yanovskaya, T. B. (2000), Development of methods for surface wave tomography based on the Backus-Gilbert approach, in *Computational Seismology and Geodynamics*, vol. 7, pp. 5–16, AGU.
- Zhao, D. (2004), Global tomographic images of mantle plumes and subducting slabs: Insight into deep Earth dynamics, *Phys. Earth Planet. Inter.*, *146*(1–2), 3–34.
- Zhao, D., and E. Ohtani (2009), Deep slab subduction and dehydration and their geodynamic consequences: Evidence from seismology and mineral physics, *Gondwana Res.*, *16*, 401–413.
- Zhao, D., S. Maruyama, and S. Omori (2007), Mantle dynamics of Western Pacific and East Asia: Insight from seismic tomography and mineral physics, *Gondwana Res.*, *11*, 120–131.
- Zheng, Y., W. Shen, L. Zhou, Y. Yang, Z. Xie, and M. Ritzwoller (2011), Crust and uppermost mantle beneath the North China Craton, northeastern China, and the Sea of Japan from ambient noise tomography, *J. Geophys. Res.*, *116*, B12312, doi:10.1029/2011JB008637.
- Zhu, H., E. Bozdağ, and J. Tromp (2015), Seismic structure of the European upper mantle based on adjoint tomography, *Geophys. J. Int.*, *201*, 18–52.